CHEMISTRY
AN ASIAN JOURNAL

DOI: 10.1002/asia.201100483

VIP

Photodissociation Dynamics of Benzaldehyde (C_6H_5CHO) at 266, 248, and 193 nm

Arnab Bagchi,[a, b] Yu-Hsuan Huang,[c] Z. F. Xu,[d] P. Raghunath,[c] Yuan T. Lee,[a] Chi-Kung Ni,*[a, e] M. C. Lin,*[c, d] and Yuan-Pern Lee*[a, c]

Abstract: The photodissociation of gaseous benzaldehyde (C_6H_5CHO) at 193, 248, and 266 nm using multimass ion imaging and step-scan time-resolved Fourier-transform infrared emission techniques is investigated. We also characterize the potential energies with the CCSD(T)/6-311+G(3df,2p) method and predict the branching ratios for various channels of dissociation. Upon photolysis at 248 and 266 nm, two major channels for formation of HCO and CO, with relative branching of 0.37:0.63 and 0.20:0.80, respectively, are observed. The C_6H_5+HCO channel has two components with large and small recoil velocities; the rapid component with average translational energy of approximately 25 kJ mol^{-1} dominates. The C_6H_6+CO channel has a similar distribution of translational energy for these two components. IR emission from internally excited C_6H_5CHO, ν_3 ($v=1$) of HCO, and levels $v\leq 2$, $J\leq 43$ of CO are observed; the latter has an average rotational energy of approximately 13 kJ mol^{-1} and vibrational energy of approximately 6 kJ mol^{-1}. Upon photolysis at 193 nm, similar distributions of energy are observed, except that the C_6H_5+HCO channel becomes the only major channel with a branching ratio of 0.82 ± 0.10 and an increased proportion of the slow component; IR emission from levels ν_1 ($v=1$) and ν_3 ($v=1$ and 2) of HCO and $v\leq 2$, $J\leq 43$ of CO are observed; the latter has an average energy similar to that observed in photolysis at 248 nm. The observed product yields at different dissociation energies are compared to statistical-theory predicted results based on the computed singlet and triplet potential-energy surfaces.

Keywords: benzaldehyde · computational chemistry · photochemistry · photolysis · time-resolved spectroscopy

Introduction

Aromatic aldehydes are emitted into the atmosphere as primary pollutants from the exhaust of motor vehicles.[1] They are also produced in the atmosphere as intermediates in the photooxidation of alkyl aromatic compounds.[2–6] Among them, benzaldehyde (C_6H_5CHO) is the smallest yet the most important.[7] In the atmosphere, the main destruction of aromatic aldehydes occurs by photodissociation with solar radiation and reactions with OH, NO_3, and O_3. The former process plays an important role in aerosol formation,[8] whereas the latter reactions in the atmosphere lead to formation of benzoylperoxyradicals, $C_6H_5C(O)OO$, an important intermediate of atmospheric pollutants.[3,6,9]

The ultraviolet (UV) spectra of gaseous C_6H_5CHO have been studied experimentally[10–13] and theoretically.[14–15] Four systems were recorded, with intensities increased with increasing excitation energy. The weak $S_1(n\pi^*)\leftarrow S_0$ system shows a well-resolved structure in the region 290–379 nm; the most intense feature of this system near 371 nm (322 kJ mol^{-1}) is established as the origin.[10–11] The other

[a] A. Bagchi, Y. T. Lee, C.-K. Ni, Y.-P. Lee
Institute of Atomic and Molecular Sciences
Academia Sinica, Taipei, 10617 (Taiwan)
E-mail: ckni@po.iams.sinica.edu.tw
yplee@mail.nctu.edu.tw

[b] A. Bagchi
Molecular Science and Technology
Taiwan International Graduate Program
Academia Sinica, Taipei, 10617 (Taiwan)

[c] Y.-H. Huang, P. Raghunath, M. C. Lin, Y.-P. Lee
Department of Applied Chemistry and Institute of Molecular Science
National Chiao Tung University
Hsinchu 30010 (Taiwan)

[d] Z. F. Xu, M. C. Lin
Department of Chemistry
Emory University
Atlanta, Georgia 30322 (USA)
E-mail: chemmcl@emory.edu

[e] C.-K. Ni
Department of Chemistry
National Tsing Hua University
Hsinchu (Taiwan)

Supporting information for this article is available on the WWW under http://dx.doi.org/10.1002/asia.201100483.

three systems were proposed to be associated with transitions to ππ* states. The $S_2 \leftarrow S_0$ system of jet-cooled C_6H_5CHO has its origin near 284 nm (421 kJ mol^{-1}) and maximum intensity near 275 nm.[14] The $S_3 \leftarrow S_0$ system has its origin near 242 nm (497 kJ mol^{-1}) and maximum intensity near 232 nm.[12] The most intense system in the series showing a maximum near 195 nm (614 kJ mol^{-1}) has been little investigated.

The triplet manifold is less characterized than the singlet;[16–19] only the $T_1(n\pi^*)$ triplet state of C_6H_5CHO has been observed in the gaseous phase. The band origin of $T_1 \leftarrow S_0$ has been determined near 397 nm (301 kJ mol^{-1}).[17,20,21] The second triplet state, likely of ππ* character, lies slightly above the T_1 state,[15] and its energy relative to that of the T_1 state of C_6H_5CHO in solutions depends on the solvent.[22]

Like other aromatic carbonyl compounds, C_6H_5CHO is only weakly fluorescent but highly phosphorescent. For excitation $S_1 \leftarrow S_0$ of C_6H_5CHO at low pressure, the efficiency of intersystem crossing $S_1 \rightarrow T_1$ is near unity.[23–24] The quantum yield for phosphorescence from the T_1 state is 0.60; the quantum yield for intersystem crossing $T_1 \rightarrow S_0$ is 0.40. The phosphorescence lifetime of the T_1 ($v=0$) state at zero pressure is 7.12×10^{-4} s,[25] but it decreases as the vibrational energy increases.[19] The quantum yield of phosphorescence decreased abruptly on excitation from S_0 to S_1, S_2, and S_3 states, thus indicating disparate nonradiative processes are involved in each excited state; an intermediate state, likely a triplet state with energy greater than that of T_1, plays an important role in the quenching of S_2 and S_3 states.[26–27] Hirata and Lim reported a monotonic decrease of the quantum yield for phosphorescence of benzaldehyde with increasing excitation wavenumber.[28] The small quantum yield of phosphorescence for states with higher energy indicates that significant nonradiative processes, including internal conversion and intersystem crossing to lower states and dissociation, occur upon excitation to these states.

Four possible channels of decomposition of C_6H_5CHO are considered as Reactions (1–4):

$$C_6H_5CHO(^1A') \rightarrow C_6H_6 + CO \quad (1)$$

$$\rightarrow C_6H_4CO + H_2 \quad (2)$$

$$\rightarrow C_6H_5CO + H \quad (3)$$

$$\rightarrow C_6H_5 + HCO \quad (4)$$

From the available experimental enthalpies of formation of the species, $\Delta_f H_{0°}(C_6H_5CHO) = -36.4$ kJ mol^{-1},[29] $\Delta_f H_{0°}(C_6H_6) = 82.8$ kJ mol^{-1},[30] $\Delta_f H_{0°}(C_6H_5) = 339.7$ kJ mol^{-1},[31] $\Delta_f H_{0°}(C_6H_5CO) = 109.2$ kJ mol^{-1},[32] $\Delta_f H_{0°}(HCO) = 43.5$ kJ mol^{-1},[33] $\Delta_f H_{0°}(CO) = -110.5$ kJ mol^{-1},[31] and $\Delta_f H_{0°}(H) = 218.0$ kJ mol^{-1},[33] the enthalpies of reaction for Reactions (1), (3), and (4) are derived to be 8.8, 363.6, 419.7 kJ mol^{-1}, respectively.

No photodecomposition of C_6H_5CHO has been observed upon excitation at 365 nm to the S_1 state.[34] Previous experiments in a static cell[35] indicated production of C_6H_6 and CO upon photoexcitation to its S_2 state with 276 nm light. The quantum yield of C_6H_6 was found to be approximately 0.9 for benzaldehyde at 0.010 Torr; it decreases with increasing pressure and the yield of phosphorescence increases accordingly. The independence of quantum yield for formation of C_6H_6 on added O_2 indicates that the dissociation occurs through a molecular channel rather than through radical intermediates.[16] This direct dissociation channel was verified in experiments in which a mixture of C_6D_5CDO and C_6H_5CHO was photolyzed; only C_6H_6 and C_6D_6 were identified.[34] The rate of relaxation for C_6H_5CHO from its S_2 state is rapid according to the photoacoustic spectra, thereby indicating that the photoproducts are stable molecules that do not react further.[35] In contrast, the S_3 state of C_6H_5CHO decays rapidly to yield radicals that recombine slowly because of their small concentrations.[35]

In experiments using a laser beam at 266 nm for multiphoton dissociation and ionization of C_6H_5CHO, a $C_6H_6^+$ signal was observed when the pulse width of the laser was 8 ns, but no signal was observed with 25 ps pulses,[36–37] indicating that the generation of $C_6H_6^+$ requires a few ns. In a similar experiment using a laser beam with a pulse width of 2 ns,[38] $C_6H_6^+$ was detected upon excitation of C_6H_5CHO at 258.9 nm but not at 258.7 nm; the ground-state C_6H_6 has a resonant absorption at 258.9 nm, but not at 258.7 nm.[38] This experiment indicates that at least some C_6H_6 in its ground state is produced from dissociation of C_6H_5CHO excited to the S_2 state.

Upon excitation to the S_2 state, a biexponential decay of the benzaldehyde signal was observed in a two-color laser-ionization mass-spectrometric experiment of C_6H_5CHO.[39] Predissociation occurs from a short-lived ($\tau \sim$ hundreds ns)

Abstract in Chinese:

我們利用多重質量離子影像儀及時間解析的紅外放光光譜研究安息香醛在波長 193，248，266 奈米的光分解動態學，並利用 CCSD(T)/6-311+G(3df,2p) 的計算方法計算分子的位能曲面及各種光分解途徑。實驗顯示在波長 248 及 266 奈米，兩個主要分解途徑是產生碎片 HCO 及 CO。它們在這兩個波長的相對產率比分別是 0.37：0.63 及 0.20：0.80。這兩個分解途徑的碎片動能分佈都具有兩個分佈，一為動能較小、一為動能較大（平均 25kJ mol^{-1}），其中以動能較大者為主要分解途徑。紅外放光光譜則觀察到由 HCO ν_3 ($v=1$), CO $v \le 2, J \le 43$ 的放光。其中 CO 的平均轉動能為~13 kJ mol^{-1}，平均振動能為~6 kJ mol^{-1}。波長 193 奈米的光分解途徑和其他波長相似，但產生碎片 HCO 的相對產率則上昇至 0.82，同時碎片具較小動能的比率也增加。紅外放光光譜則觀察到由 HCO ν_1 ($v=1$) 及 ν_3 ($v=1$ 和 2)，CO $v \le 2, J \le 43$ 的放光。其中 CO 的平均轉動能和平均振動能都和波長 248 奈米的光分解相似。最後我們將這些實驗結果和利用統計理論的方法計算分子在單重態或參重態位能面上的分解途徑做一比較。

intermediate state with a threshold for dissociation smaller than the energy of the S_2 state of C_6H_5CHO; the other intermediate state is a long-lived ($\tau > 10^{-6}$ s) triplet state. As the photon energy of the probe pulse (157 nm) is large enough only to ionize C_6H_6 in its electronically excited states, the signal of benzene ions is believed to be as a result of its triplet state. The existence of a second channel leading to C_6H_6 in its ground electronic state has been suggested as an enhancement of the benzene signal was observed at excitation energies corresponding to the allowed transition $S_1 \leftarrow S_0$ of C_6H_6.[39]

Radical products from S_2 were reported only once, upon photolysis of gaseous C_6H_5CHO with laser emission at 280, 285, and 308 nm.[40] HCO radicals were detected with cavity-ringdown absorption; the quantum yield was estimated to be 0.3–0.4, depending on the wavelength of excitation. Park and co-workers suggested, however, that the HCO radicals found in the previous work were likely generated from multiphoton processes.[41] They employed ultrafast electron diffraction with temporal resolution of 1 ps to investigate the dynamics of C_6H_5CHO upon excitation at 266.7 nm to the S_2 state and found that internal conversion to S_1 occurred within 250 fs, followed by bifurcation: the singlet channel leads to singlet dissociation products C_6H_6+CO and the intersystem crossing from the S_1 to the T_2 state followed by quenching to the T_1 state leads to phosphorescence and the formation of CO and triplet C_6H_6.[41]

Shin and co-workers employed laser emission at 243 nm for photolysis of C_6H_5CDO and detected the fluorescence of H (or D) atoms with two-photon excitation.[42] They measured a translational energy release of 74.2 and 82.7 kJ mol^{-1} for H and D, respectively, and proposed that the two-photon absorption of C_6H_5CDO leads to formation of primarily C_6H_5 and DCO; the latter further decomposes into CO and D.

In this work we investigated the photodissociation of gaseous C_6H_5CHO at 193, 248, and 266 nm using multimass ion imaging and time-resolved infrared (IR) emission techniques. We measured the distributions of translational energy of photofragments and of vibrational and rotational states of CO and HCO, characterized the PES with quantum-chemical calculations, and evaluated the branching ratios for various dissociation channels.

Results

A. Dissociation Channels and Translational Energy Distributions

I. Photolysis at 193 nm

The ion images of photofragments with $m/z = 29$, 77, and 78 obtained upon photodissociation of C_6H_5CHO at 193 nm is shown in Figure S1 in the Supporting Information.[43] These fragments were produced through one-photon dissociation with laser fluence in the range 0.5–3.9 mJ cm^{-2}. The images for $m/z = 77$ and 29 correspond to products C_6H_5 and HCO, respectively, from Reaction (4). The image of $m/z = 78$ represents product C_6H_6 from Reaction (1). We paid special attention to search for fragment C_6H_5CO from Reaction (3), but only a small proportion of parent molecules fragments into $C_6H_5CO^+$ upon ionization with photons at 118 nm. According to the pertinent S/N ratio, the ion intensity of $C_6H_5CO^+$ produced from Reaction (3) is less than 1% of the ion intensity of $C_6H_5^+$ produced from Reaction (4). The fragment C_6H_5CO likely decomposes further into C_6H_5+CO.

The momentum distributions for $m/z = 77$ and 29, shown in Figure 1a, match poorly in the region between $\pm 0.5 \times 10^{-22}$ kg m s^{-1}. The difference arises from several possible secondary dissociation channels, including Reactions (5–7)

$$C_6H_5CO \rightarrow C_6H_5 + CO \quad (5)$$

$$C_6H_6 \rightarrow C_6H_5 + H \quad (6)$$

$$HCO \rightarrow H + CO \quad (7)$$

The momentum distribution for $m/z = 29$ clearly shows a bimodal distribution, indicating two dissociation mechanisms for the HCO elimination channel. We found that the population of the slow component is only 3% of the fast component after a calibration of the sensitivity; fragments with small recoil velocity are more sensitively detected by our set-up. The distribution of translational energy of photofragments in this channel is shown in Figure 1b; the average translational energy is 30 kJ mol^{-1}.

The intensity ratio between fragment $m/z = 77$ and fragment $m/z = 78$ is about 8.7:1.0, which indicates that more than half the signal at $m/z = 78$ is a result of fragment C_6H_5 containing a single ^{13}C according to natural abundance. The translational energy distribution of fragments in the C_6H_6+CO channel, shown in Figure 1c, was derived after subtraction of 6.6% intensity of $m/z = 77$ from $m/z = 78$; the average translational energy is 38 kJ mol^{-1}.

Fragments with $m/z = 39$, 50, 51, and 52 were also observed, but their intensities were only about 1–5% that of $m/z = 77$. They have a velocity distribution similar to that of $m/z = 77$, indicating that a small fraction of fragments with $m/z = 77$ breaks into these fragments (C_3H_3, C_4H_2, C_4H_3, C_4H_4) upon ionization at 118 nm.

As we did not observe C_6H_5CO radicals, the branching ratio for the dissociation channel $C_6H_5CHO \rightarrow C_6H_5CO$+H is estimated from the difference in momentum distributions between signals at $m/z = 77$ and 29. Since the difference is small, as shown in Figure 1a, if only the difference is attributed to the decomposition of C_6H_5CO into C_6H_5+CO, the relative branching ratios for elimination of the H atom and HCO are 0.05:0.82.

The branching ratios for Reactions (4) and (1) are estimated as follows. In the photodissociation of nitrosobenzene, a major channel is $C_6H_5NO \rightarrow C_6H_5$+NO. The ratio of intensities of ions $C_6H_5^+$ and NO^+ measured at the same VUV wavelength (118.2 nm) is 32:1. As these two fragments result from the same dissociation channel of nitrosobenzene

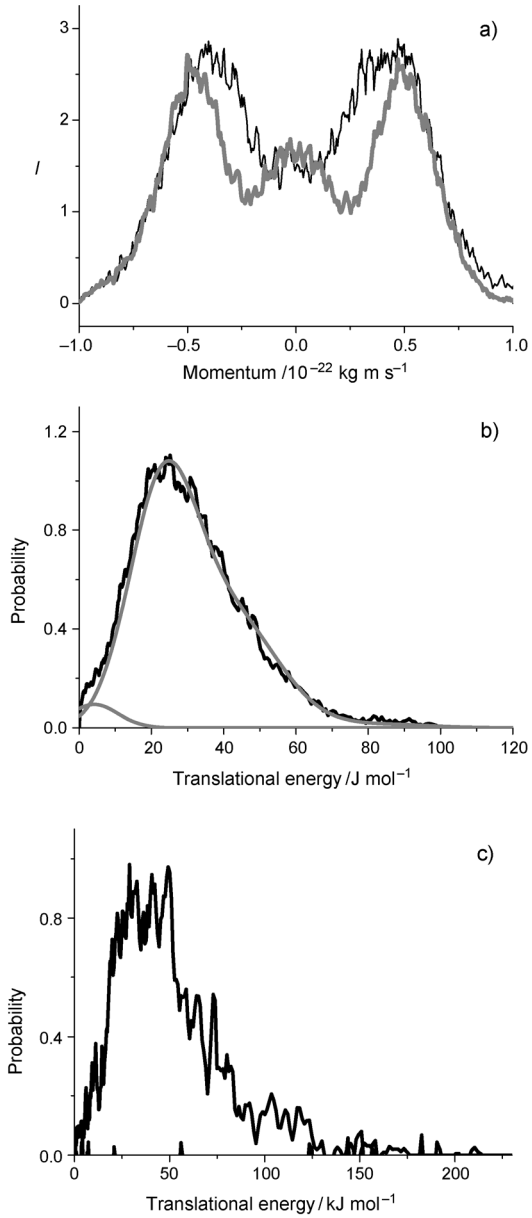

Figure 1. a) Momentum distribution of $m/z=29$ (gray) and $m/z=77$ (black) and b) translational energy distributions of photofragments from photolysis of C_6H_5CHO at 193 nm for channels $C_6H_5CHO \rightarrow C_6H_5$+HCO and c) $C_6H_5CHO \rightarrow C_6H_6$+CO. The gray curves in (b) represent two components in the distribution of translational energy.

and as the VUV photon energy is much greater than the ionization threshold of these two fragments, the ratio of ion intensity yields a satisfactory estimate of the ratio of ionization cross sections of these two fragments at this wavelength. In a separate experiment, the ratio of cross sections for ionization of C_6H_6 and NO was measured directly from the corresponding ion intensity of a gas mixture (C_6H_6 at 5 Torr and NO at 5 Torr diluted with He at 400 Torr). The ratio of ion intensities of $C_6H_6^+$ and NO^+ is 14:1. These ratios of ionization cross sections allow calculation of the branching ratio. As a result, the branching ratios for formation of HCO, CO, and H, corresponding to Reactions (4), (1), and (3), are 0.82:0.12:0.05.

We have measured the ion intensities of products as a function of delay between the pulses of the pump laser and the probe laser. These intensities remained nearly constant for delays between 100 ns–2 μs, thus indicating that the rate coefficient for dissociation is greater than 10^7 s^{-1}.

II. Photolysis at 248 nm

The photofragment ions obtained upon irradiation of C_6H_5CHO at 248 nm are similar to those obtained at 193 nm, but with different relative intensities. These fragments were produced through one-photon dissociation with laser fluence in the range 1.1–8.6 mJ cm^{-2}. Ion images of these photofragments are shown in Figure S2 in the Supporting Information.[43] Images of both $m/z=77$ and 78 at small delays contain two components, a disk-like image and a linear image. The disk-like image represents the fragmenting ionization of excited C_6H_5CHO or its heavy fragments like C_6H_5CO by VUV photons. The linear image for $m/z=77$ represents fragment C_6H_5 produced from dissociation before ionization with VUV photons. The momentum distribution of the signal at $m/z=29$ in Figure 2a also shows two components, although the second component is less clear than that observed in photolysis at 193 nm. The momentum distribution for $m/z=77$ matches well with that for $m/z=29$ for the portion of the linear image, as shown in Figure 2a, indicating that these fragments are produced from the dissociation channel $C_6H_5CHO \rightarrow C_6H_5$+HCO, but the central part of the linear image is obscured by the disk-like image such that a match of momentum distribution cannot be verified.

As the delay increases, the linear component for $m/z=77$ flies away from the detection region and a second linear component appears, whereas the intensity of the disk-like image becomes small, as illustrated in Figure S2c in the Supporting Information.[43] Owing to the second linear component having a small velocity, it is buried in the disk-like component at a small delay and can be observed only at a long delay. Possible secondary reactions responsible for the slow component include Reactions (5) and (6). The disk-like image representing the fragmenting ionization of excited C_6H_5CHO by VUV photons was observed even at a long delay, indicating that some excited parent molecules are in a metastable state and hence do not dissociate completely into fragments even after 100 μs.

The ratio of ion intensities for $m/z=77$ to $m/z=78$ is 1:0.8, indicating that most of the signal for $m/z=78$ results from the dissociation products C_6H_6+CO, with a small contribution from fragment C_6H_5 containing a single ^{13}C according to natural abundance. The translational energies of photofragments corresponding to channels C_6H_5+HCO and C_6H_6+CO are shown in Figure 2b and 2c, respectively; the average translational energies are 25 and 27 kJ mol^{-1}, respectively. Fragments with $m/z=39$, 50, 51, and 52 are also observed, but their intensities are less than 1% of that with $m/z=77$.

CHEMISTRY
AN ASIAN JOURNAL

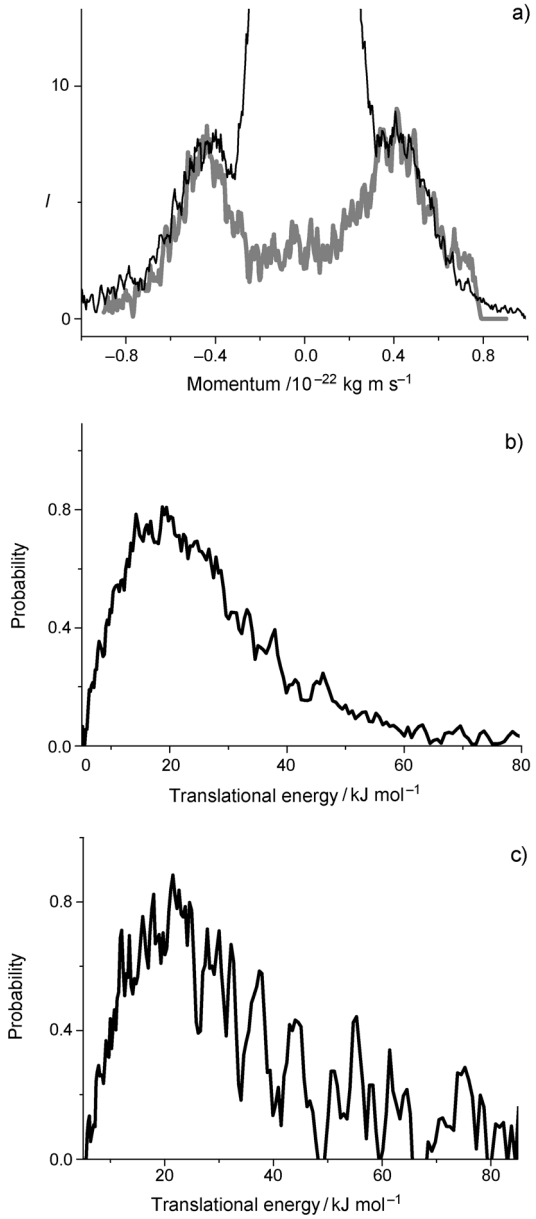

Figure 2. a) Momentum distribution of $m/z=29$ (gray) and $m/z=77$ (black) and b) translational energy distributions of photofragments from photolysis of C_6H_5CHO at 248 nm for channels $C_6H_5CHO \rightarrow C_6H_5$+HCO and c) $C_6H_5CHO \rightarrow C_6H_6$+CO.

The branching ratio of Reaction (4) to Reaction (1), calculated using the method described in the preceding section, is 1.0 ± 0.1:1.7 ± 0.1. However, the fragment C_6H_5CO generated from Reaction (3), H-atom elimination, can easily break into smaller ionic fragments such as $C_6H_5^+$+CO upon ionization; the corresponding image is overlapped with the disk-like image. Fragment C_6H_5 generated from three-body dissociation, such as $C_6H_5CHO \rightarrow C_6H_5CO+H \rightarrow C_6H_5$+CO+H, was also obscured by the disk-like image. As a result, neither the photofragment translational energy nor the relative branching ratio for the H-atom elimination channel can be determined.

III. Photolysis at 266 nm

The ion images obtained upon irradiation of C_6H_5CHO at 266 nm are similar to those obtained at 248 nm, but with different relative intensities. Ion images of these photofragments are shown in Figure S3 in the Supporting Information.[43] As the absorption cross section of benzaldehyde at 266 nm is much smaller than that at 248 and 193 nm, a larger laser fluence at this wavelength is necessary to obtain a satisfactory S/N ratio. The fluence dependence of these fragments was tested in the range 5–40 mJ cm^{-2}. The ion image for $m/z=29$ and the portion of disk-like images for $m/z=77$ and 78 result from one-photon absorption. In contrast, the ratios of the linear image intensity to the disk-like image intensity for $m/z=77$ and 78 are 0.03 and 0.16, respectively, at laser fluence of 5 mJ cm^{-2}, and become 0.06 and 0.22 at laser fluence of 40 mJ cm^{-2}. A small fraction of linear images thus arises from two-photon absorption in the latter case.

Two components in the momentum distribution for $m/z=29$ were also observed at this photolysis wavelength. The match of momentum distributions between $m/z=29$ and the portion of linear image for $m/z=77$, as shown in Figure 3a, indicates that they are produced from Reaction (4). The translational energy of photofragments corresponding to channels C_6H_5+HCO and C_6H_6+CO are shown in Figure 3b and 3c, respectively; they were taken from the images measured at the smallest laser fluence (5 mJ cm^{-2}) to decrease interference from two-photon absorption. The average translational energies are 20 and 22 kJ mol^{-1}, respectively. The branching ratio of Reaction (4) to Reaction (1) was found to be 1.0 ± 0.1:4.1 ± 0.3.

B. Infrared Emission

In TR-FTS experiments, to maintain a nearly collisionless condition within a 1-μs period, the partial pressure of C_6H_5CHO and He were decreased as much as practicable while maintaining a satisfactory S/N ratio. The reported absorption cross section of C_6H_5CHO at 248 nm is 1.6×10^{-18} cm^2 molecule^{-1}.[44] Since no corresponding value at 193 nm is reported, we estimated it with a power meter to be approximately 2.6×10^{-17} cm^2 molecule^{-1}. The power dependence of the emission signals was tested; the order of power dependence was determined to be 0.99 ± 0.01 for light at 193 nm for fluence <30 mJ cm^{-2} and 1.09 ± 0.05 for light at 248 nm for fluence <120 mJ cm^{-2}.

I. Photolysis at 193 nm

Figure 4a–c shows survey emission spectra in the spectral region 1850–3900 cm^{-1} recorded at the first three 5-μs intervals upon photolysis of a mixture of C_6H_5CHO (31 mTorr) and He (24 mTorr) at 193 nm; spectral resolution is 6 cm^{-1}. The IR emission in the region 2000–2300 cm^{-1} is assigned to the P and R branches of CO and those in regions 1850–1950 cm^{-1} and 2300–2600 cm^{-1} are assigned to the C=O stretching and C–H stretching modes of HCO, respectively.

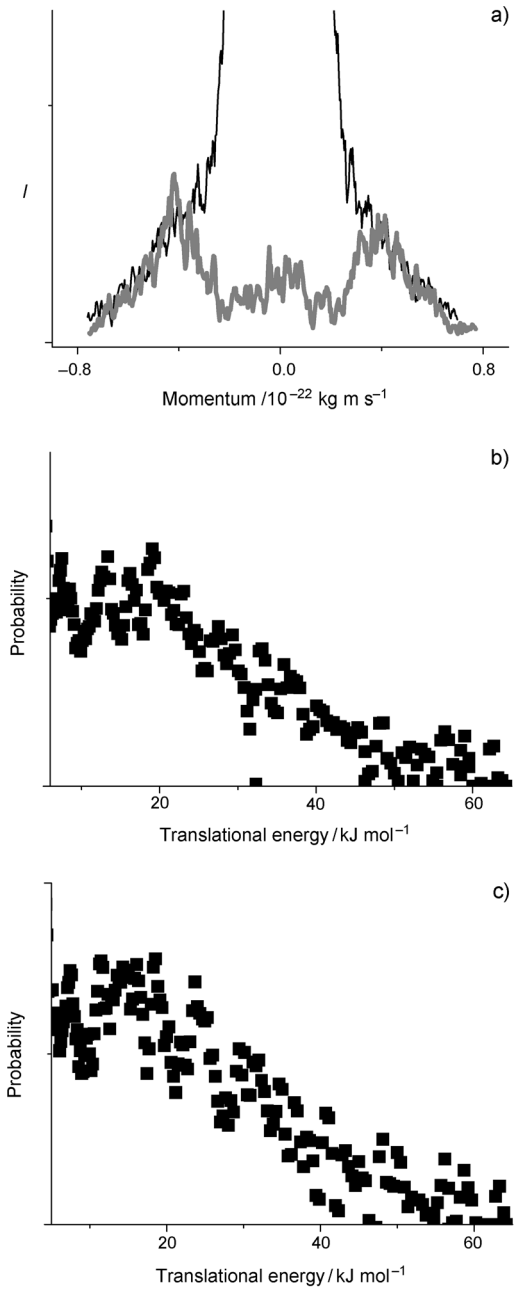

Figure 3. a) Momentum distribution of $m/z=29$ (gray) and $m/z=77$ (black) and b) translational energy distributions of photofragments from photolysis of C_6H_5CHO at 266 nm for channels $C_6H_5CHO \rightarrow C_6H_5$+HCO and c) $C_6H_5CHO \rightarrow C_6H_6$+CO.

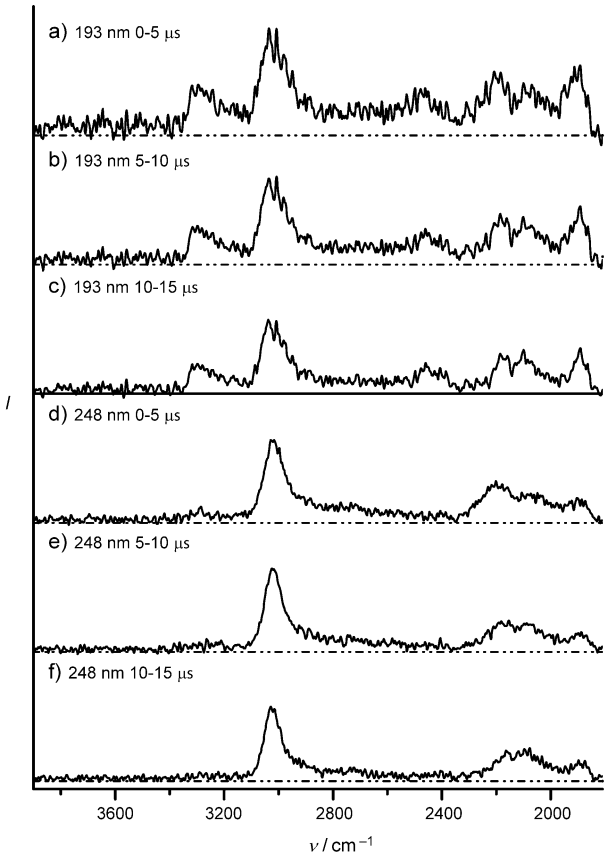

Figure 4. IR emission spectra in spectral region 1850–3900 cm^{-1} recorded a) 0–5 μs, b) 5–10 μs, and c) 10–15 μs upon photolysis of a flowing mixture of C_6H_5CHO (31 mTorr) and He (24 mTorr) at 193 nm. IR emission spectra recorded d) 0–5 μs, e) 5–10 μs, and f) 10–15 μs upon photolysis of a flowing mixture of C_6H_5CHO (25 mTorr) and He (50 mTorr) at 248 nm. Spectral resolution is 6 cm^{-1}; 60 laser pulses were averaged at each scan step.

Two bands in the region 2830–3360 cm^{-1} are likely to be assigned to the C−H stretching modes of C_6H_5CHO and/or its dissociation products.

Infrared Emission of CO: An emission spectrum of CO recorded at resolution of 0.4 cm^{-1} and 0–1 μs after photolysis of C_6H_5CHO in He is available in Figure S4 in the Supporting Information;[43] vibration–rotational assignments based on spectral parameters reported by Ogilvie and coworkers[45] are shown. Emission of CO from levels $J \leq 43$ and $v \leq 2$ was observed. Each vibration–rotational line in the P and R branches was normalized with the instrument-response function, and divided by its respective Einstein coefficient[46] to yield a relative population $P_v(J)$, in which v and J represent vibrational and rotational quantum numbers of the upper states. The averaged relative populations of P and R branches were used to improve the quality of the data. Semi-logarithmic plots of $P_v(J)/(2J+1)$ versus E_{rot} (in cm^{-1}) for CO ($v=1$ and 2, symbol ○), derived from the spectrum recorded in the range 0–1 μs, are shown in Figure 5. Fitted Boltzmann-like rotational distributions of CO yield similar rotational temperatures, 1920 ± 40 and 1730 ± 80 K, for $v=1$ and 2, respectively; unless specified, listed error limits represent single standard deviations in fitting. The average rotational energy $E_r = 12.6 \pm 1.4$ kJ mol^{-1} was derived for CO ($v=1$–2) observed 0–1 μs after photolysis. Similar procedures were undertaken for spectra averaged over 1–2, 2–3, and 3–4 μs and rotational temperatures of 1780 ± 40, 1670 ± 40, and 1540 ± 40 K were derived for $v=1$; 1570 ± 90, 1530 ± 90, and $12\,805 \pm 50$ K were derived for $v=2$, respectively. With a short extrapolation from these data, we estimate the nascent rotational temperature to be

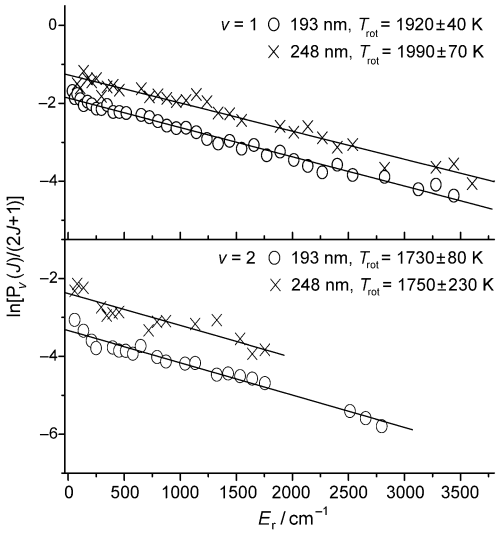

Figure 5. Semi-logarithmic plots of relative rotational populations of CO ($v=1$ and 2) upon photolysis of a flowing mixture of C_6H_5CHO (31 mTorr) and He (24 mTorr) at 193 nm (○) and a flowing mixture of C_6H_5CHO (37 mTorr) and He (75 mTorr) at 248 nm (×). Solid lines represent least-square fits. The lines are displaced for clarity.

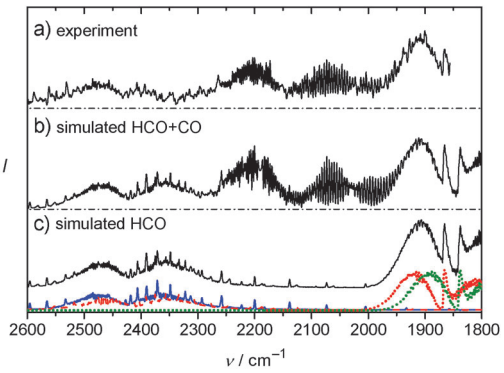

Figure 6. Comparison of observed and simulated spectra in the region 1800–2600 cm^{-1} at resolution of 2 cm^{-1}. a) IR emission spectra recorded 0–2 μs upon photolysis of a flowing mixture of C_6H_5CHO (31 mTorr) and He (24 mTorr) at 193 nm. 60 laser pulses were averaged at each scan step and 4 spectra recorded under similar conditions were averaged. b) Simulated spectrum consisting of emission from HCO with a rotational temperature around 1300 K and CO with a rotational temperature around 1900 K; bandwidth is 2 cm^{-1}. c) Simulated spectrum of HCO showing each component. Red dotted line: (001)–(000) with $\nu_0=1868.2$ cm^{-1}; green dotted line: (002)–(001) with $\nu_0=1840.8$ cm^{-1}; blue solid line: (100)–(000) with $\nu_0=2434.5$ cm^{-1} and a-type/b-type = 0.66/0.34; red dashed line: (101)–(010) with $\nu_0=2413.5$ cm^{-1}.

1990±90 K and 1840±130 K for $v=1$ and 2, respectively. After applying a correction factor of 1.05 (average of 1990/1920 = 1.04 and 1840/1730 = 1.06) for rotational quenching, we derive a nascent rotational energy of 13±2 kJ mol^{-1}; the listed uncertainty represents an estimated single standard error after consideration of the quenching.

We assumed a Boltzmann rotational distribution and associated an interpolated population for overlapped lines. Relative populations obtained on counting levels up to the observed J_{max} in each vibrational level were normalized to yield relative vibrational populations $(v=1)/(v=2)=84:16$, which correspond to a vibrational temperature of 1880± 130 K. Assuming a Boltzmann vibrational distribution, we estimated normalized vibrational distribution of CO as $(v=0)/(v=1)/(v=2)=81.2:15.6:3.2$. When the population of the $v=0$ level is estimated according to the surprisal analysis, the distribution is $(v=0)/(v=1)/(v=2)=79.9:16.7:3.4$, similar to that estimated from the Boltzmann distribution. The average vibrational energy of CO thus derived is $E_v=6\pm$ 2 kJ mol^{-1}; the listed uncertainty is estimated from the errors in estimates of the vibrational population.

Infrared Emission of HCO: Figure 6a shows the emission spectrum in the spectral region 1850–2600 cm^{-1} recorded at a resolution of 2 cm^{-1} and 0–2 μs upon photolysis of a mixture of C_6H_5CHO (31 mTorr) and He (24 mTorr) at 193 nm. Emission of CO in the range 1950–2250 cm^{-1} is discussed in the preceding section; the origins of the two additional bands that we observed in this region coincide with values 1868.17 and 2434.48 cm^{-1} of the C=O stretching (ν_3) and the C–H stretching (ν_1) bands of HCO, respectively.[47–48] The mode numbering follows that of McKellar and co-workers.[49] To confirm these assignments, we employed the PGopher program[50] to simulate the emission spectrum with spectral parameters from the literature, as listed in Table SI in the Supporting Information.[48,49,51] We varied the intensity ratio for levels $(v=1)/(v=2)$ and rotational temperature to obtain the best fit for the C=O stretching region. The simulated spectrum of HCO is shown as solid lines in Figure 6c, with red and green dotted lines showing the a-type emission components from transitions of the C=O stretching mode (001)–(000) and (002)–(001) of HCO, respectively. The spectral parameters for level $v=2$ were calculated from a formula of form A_v (or B_v, C_v) = A_e (or B_e, C_e) + α (v+1/2) with $A_e=24.38021$ cm^{-1}, $\alpha^A=-0.10123$ cm^{-1}, $B_e=1.50022$ cm^{-1}, $\alpha^B=-0.01253$ cm^{-1}, $C_e=1.40440$ cm^{-1}, and $\alpha^C=-0.01147$ cm^{-1}.[49] A rotational temperature of approximately 1300 K for both bands and an intensity ratio for (002)/(001)≅1/1 of the C=O stretching mode provide the best fit.

We simulated the C–H stretching region similarly. The solid line in the spectral region 2200–2600 cm^{-1} of Figure 6c represents a spectrum of the C–H stretching mode of HCO with a hybrid type having a-type/b-type = 0.66:0.34, simulated based on parameters derived from the literature; the blue and red dotted lines indicate the components from transitions (100)–(000) and (101)–(001), respectively. A rotational temperature of 1300 K and an intensity ratio of (101)/(100) = 19:28 provide the best fit. Figure 6b shows a simulated spectrum consisting of emission from CO and HCO. The agreement between experiments and simulation is satisfactory, except that relative intensities of certain branches in the simulated C–H stretching region of HCO deviates somewhat.

Emission in Spectral Region 2800–3360 cm^{-1}: Figure 7a shows an emission spectrum recorded between 0–20 μs upon photolysis of a mixture of C_6H_5CHO (31 mTorr) and He (24 mTorr) at 193 nm; two broad emission bands are ob-

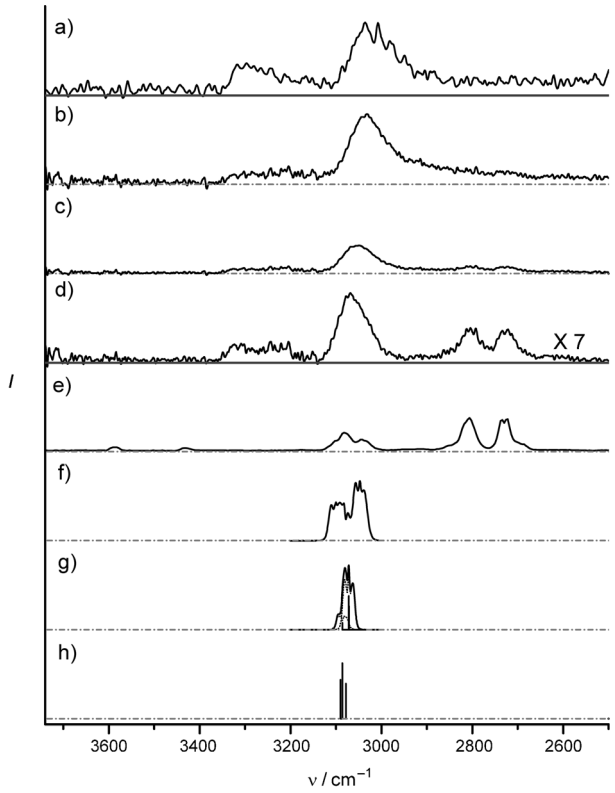

Figure 7. Comparison of IR emission spectra in spectral region 2600–3430 cm^{-1} recorded under varied conditions. a) Photolysis of a flowing mixture of C_6H_5CHO (31 mTorr) in He (24 mTorr) at 193 nm in time period 0–25 μs and b) photolysis of a flowing mixture of C_6H_5CHO (45 mTorr) and Ar (1.7 Torr) at 193 nm in time periods 0–25 μs, c) 25–50 μs, and d) 50–75 μs. Spectral resolution is 4 cm^{-1}; 60 laser pulses were averaged at each scan step. e) Absorption spectrum of C_6H_5CHO in a static cell at 300 K and f) C_6H_6 in a static cell at 300 K. g) Simulated spectrum of C_6H_5 (ν_{19} and ν_1 modes) at 300 K; observed lines of C_6H_5 in an Ar matrix[63] are shown as black sticks. h) Stick spectrum of unscaled fundamental vibrational wavenumbers of C_6H_5CO computed at the B3LYP/6-311G** level.

served with maximum intensities near 3031 and 3317 cm^{-1} and full widths at half maximum (FWHM) of 130 and 100 cm^{-1}, respectively. Figure 7 b–d show emission spectra recorded during the first three 25-μs intervals upon photolysis of a mixture of C_6H_5CHO (45 mTorr) and Ar (1.7 Torr) at 193 nm; the added Ar gas was intended to thermalize the rotational distribution of the emitting species. The emission band near 3300 cm^{-1} is stronger in the low-pressure condition. As time progressed, the maximum of the broad feature in region 2830–3110 cm^{-1} shifted from 3031 to 3069 cm^{-1}, and two broad features with maxima near 2730 and 2806 cm^{-1} became clear. These new features and part of the broad feature in the region 3000–3100 cm^{-1} are likely to be a result of emission of C_6H_5CHO as they resemble the absorption spectrum of C_6H_5CHO at 300 K shown in Figure 7 e.

A reported absorption spectrum of C_6H_6 at 300 K and 0.76 Torr is shown in Figure 7 f;[52] the C–H stretching (ν_{12}) band is near 3048 cm^{-1}, and its combination bands $\nu_{13}+\nu_{16}$, $\nu_2+\nu_{13}+\nu_{18}$, and $\nu_3+\nu_{10}+\nu_{18}$ are at 3079, 3100, and 3102 cm^{-1}, respectively. A simulated absorption spectrum of C_6H_5 at 300 K based on reported spectral parameters[53–54] and relative intensity[55] is shown in Figure 7 g; two modes ν_{19} and ν_1 at 3072 and 3086 cm^{-1}, respectively, are overlapped. The IR absorption spectrum of C_6H_5 isolated in solid Ar is shown as stick diagrams with relative intensities indicated as statures of the sticks.[55] A stick spectrum of C_6H_5CO (benzoyl radical) calculated with density-functional theory at level B3LYP/6-311G** is shown in Figure 7 h; calculated wavenumbers of the C–H stretching modes of C_6H_5CO are corrected with a factor of 0.9668 to yield 3078, 3086, and 3090 cm^{-1}, respectively.

The only confirmed contributor to the emission in this region is C_6H_5CHO. For the band in region 2830–3110 cm^{-1}, contributions from emission of C_6H_6 or C_6H_5 or C_6H_5CO are possible, as they all have emission bands near this region. The band near 3320 cm^{-1} might arise from the $\nu_1+\nu_2$ combination band of HCO because its intensity correlates with those of the fundamental bands of HCO.

II. Photolysis at 248 nm

Figure 4 d–f present the emission spectra at a resolution of 6 cm^{-1} in the spectral region 1850–3900 cm^{-1} recorded at the first three 5-μs intervals upon photolysis of C_6H_5CHO (25 mTorr) in He (50 mTorr) at 248 nm. The intensities of the emission features, observed upon photolysis of C_6H_5CHO at 193 nm, near 1870, 2435, and 3320 cm^{-1} arising from HCO are greatly decreased upon photolysis at 248 nm; only the $v=1$ level of the C=O stretching mode is clearly visible.

Emission spectra of CO at a resolution of 0.4 cm^{-1}, upon photolysis of a flowing mixture of C_6H_5CHO (37 mTorr) and He (75 mTorr), are similar to those observed at 193 nm; the spectra exhibit emission from CO with $J \leq 43$ and $v \leq 2$. Semi-logarithmic plots of $P_v(J)/(2J+1)$ versus $J(J+1)$ for CO ($v=1$ and 2, symbol ×), derived from the spectrum recorded in the range of 0–1 μs, are shown in Figure 5 and compared with those obtained at 193 nm. Fitted Boltzmann-like rotational distributions of CO yielded rotational temperatures of 1990 ± 70 and 1750 ± 230 K for $v=1$ and 2, respectively; the average rotational energy is $E_r = 12 \pm 3$ kJ mol^{-1}. Similar procedures were undertaken to account for rotational quenching. With a short extrapolation from data at 1–4 μs to $t=0$, we estimate the nascent rotational temperature to be 2210 ± 130 K and 1900 ± 290 K for $v=1$ and 2, respectively. After applying a correction factor of 1.10 (average of 2210/1990 = 1.11 and 1900/1750 = 1.08) for rotational quenching, we derive a nascent rotational energy of 14 ± 4 kJ mol^{-1}, similar to that observed at 193 nm.

Assuming a Boltzmann vibrational distribution, we derived a vibrational distribution of CO as $(v=0)/(v=1)/(v=2) = 77.0:18.5:4.5$. The vibrational temperature thus derived is 2130 ± 170 K; the error reflects the estimates of the vibrational population. A vibrational distribution of CO as $(v=0)/(v=1)/(v=2) = 75.3:19.8:4.8$ was derived according to surprisal analysis. The average vibrational energy of CO is thus $E_v = 7 \pm 2$ kJ mol^{-1}.

C. Potential-Energy Surfaces and Branching Ratios from Calculations

I. Potential-Energy Surface for the Reaction

The geometries of the reactant, transition states, and products of the photodissociation of C_6H_5CHO, optimized at the B3LYP/6-311+G(3df, 2p) level of theory,[56–59] are available in Figure S5 in the Supporting Information.[43] The stationary points were identified for local minima or transition states according to vibrational analysis. The vertical excitation energies of singlet state $C_6H_5CHO(^1A')$ were calculated with time-dependent density-functional theory (TD-B3LYP)[60] using the 6-311+G(3df, 2p) basis set. The potential-energy surfaces (PES) for both singlet and triplet states were refined using the CCSD(T)/6-311+G(3df, 2p) method[61–62] based on geometries optimized at the level B3LYP/6-311+G(3df, 2p) of theory. Figure 8 displays the potential-energy surface (PES) and the vertical excitation energies of $C_6H_5CHO(^1A')$. All calculations of electronic structure were performed with the Gaussian 03 program.[63]

Singlet PES: Excitations to states S_1, S_2, S_3, S_5, and S_7 have oscillator strengths 0.0001, 0.0195, 0.2424, 0.1433, and 0.2305, respectively. The S_4 state reported in previous experiments is likely the S_5 state calculated here as the calculated S_4 and S_6 states have small oscillator strengths. Upon irradiation at 248 or 266 nm, C_6H_5CHO is excited to the S_2 state, whereas irradiation at 193 nm might produce excitation mainly to the S_5 state

Six possible channels for decomposition, Reactions (1)–(4), (8), and (9), are considered on the ground-state singlet PES for the initial reaction of $C_6H_5CHO(^1A')$.

$$C_6H_5CHO \rightarrow tC_6H_5COH \rightarrow \text{further decomposition} \quad (8)$$

$$C_6H_5CHO \rightarrow C_6H_4CHOH \rightarrow \text{further decomposition} \quad (9)$$

Excitation wavelengths at 266, 248, and 193 nm are energetically accessible for all six possible channels, but secondary decomposition to form C_6H_5+H+CO is unlikely to occur for excitation of C_6H_5CHO at $\lambda \geq 248$ nm if one considers energy partitioning among fragments in the primary step.

Reaction (1) produces C_6H_6 and CO via the transition state TS1 with a barrier of 368 kJ mol^{-1}. This three-membered CCH-ring transition state, shown in Figure S5 in the Supporting Information,[43] indicates C–C bond breaking with migration of H from the C atom of the carbonyl group to the C atom of the phenyl ring. The energy of products CO+C_6H_6 is only 2.5 kJ mol^{-1} above that of $C_6H_5CHO(^1A')$. Reaction (2) represents elimination of H_2 via TS2 to produce C_6H_4CO (benzocyclopropenone) with a barrier of 397 kJ mol^{-1} and dissociation energy of 286 kJ mol^{-1}. Reaction (3) involves elimination of H atom to produce C_6H_5CO radical with dissociation energy of 365 kJ mol^{-1}. Reaction (4) generates C_6H_5 and HCO radicals with dissociation energy of 413 kJ mol^{-1}. Both radical product channels, Reaction (3) and (4), occur via loose transition states. Subsequent decompositions of C_6H_5CO and HCO radicals to produce CO occur via transition states TS7 and TS8, respectively; the former has a reaction barrier of 98 kJ mol^{-1} and the latter 67 kJ mol^{-1}. Both channels lead to the same products C_6H_5+CO+H, which have energy 467 kJ mol^{-1} above $C_6H_5CHO(^1A')$. As mentioned in the Introduction, the enthalpies of reaction for Reactions (1), (3), and (4) are derived to be 8.8, 363.6, 419.7 kJ mol^{-1}, respectively; our calculated values of 2.5, 365.3, and 413.0 kJ mol^{-1} are consistent with these experimental values.

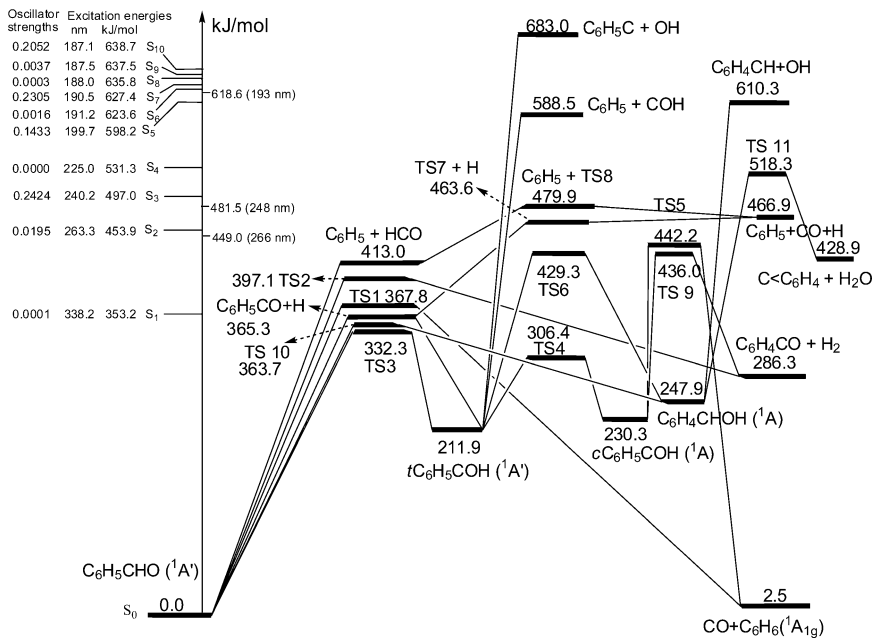

Figure 8. Vertical excitation energies of singlet states of C_6H_5CHO calculated with the TD-B3LYP/6-311+G-(3df, 2p) method and energies of transition states, intermediates, and products for the decomposition of C_6H_5CHO on the singlet surface computed at the CCSD(T)/6-311+G(3df, 2p)//B3LYP/6-311+G(3df, 2p) level.

Reaction (8) is an isomerization from $C_6H_5CHO(^1A')$ to $tC_6H_5COH(^1A')$ via the transition state TS3, at which the H atom of the carbonyl group migrates to the O atom. TS3 and $tC_6H_5COH(^1A')$ have energies greater than $C_6H_5CHO(^1A')$ by 332 and 212 kJ mol^{-1}, respectively. Following formation of $tC_6H_5COH(^1A')$, five subsequent channels are considered. First, tC_6H_5COH eliminates the hydroxy H atom to yield C_6H_5CO via a loose transition state. Second, tC_6H_5COH isomerizes into $cC_6H_5COH(^1A')$

via TS4 with a barrier of 95 kJ mol^{-1} followed by decomposition into CO+C_6H_6 and C_6H_4CO+H_2 via TS5 and TS9, respectively. The energies of TS5 and TS9 are much greater than those of TS1 and TS2. The products CO+C_6H_6 and C_6H_4CO+H_2 are hence expected to be produced mainly via TS1 and TS2. Third, $t$$C_6H_5$COH(^{1}A′) isomerizes into C_6H_4CHOH(^{1}A) via transition state TS6, which has a much greater energy than that of TS4. Further dissociation to radicals C_6H_4CH and OH has an energy of 362 kJ mol^{-1}. The remaining two channels to produce C_6H_5+COH and C_6H_5C+OH, for which the dissociation energies are 377 and 471 kJ mol^{-1}, respectively, seem unimportant.

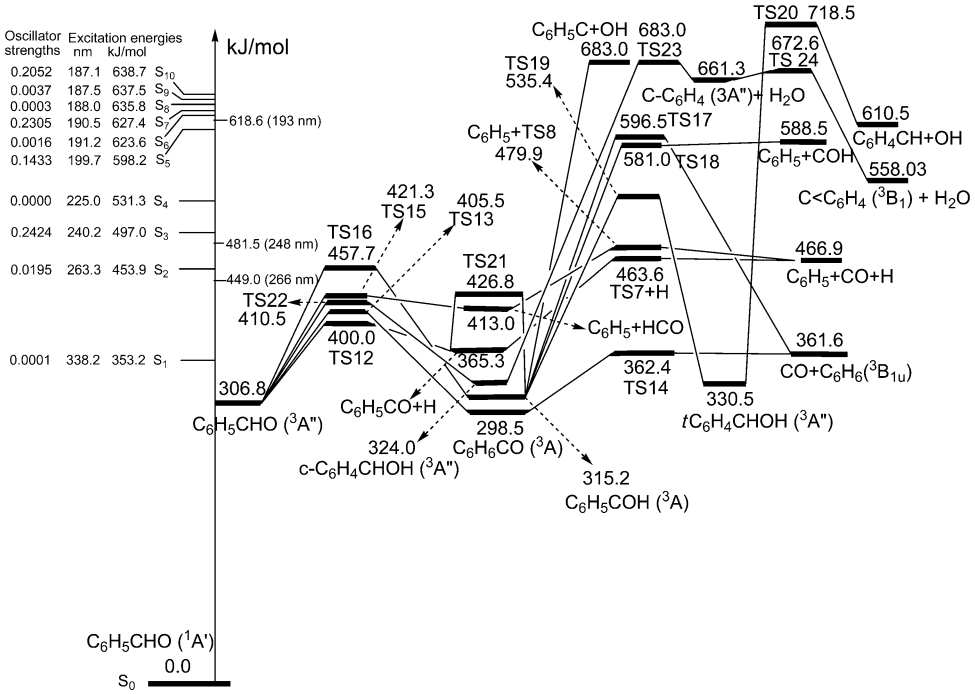

Figure 9. Energies of transition states, intermediates, and products for the decomposition of C_6H_5CHO on the triplet surface computed at the CCSD(T)/6-311+G(3df, 2p)//B3LYP/6-311+G(3df, 2p) level.

Finally, we studied the Reaction (9) which starts from isomerization of C_6H_5CHO to C_6H_4CHOH(^{1}A) simultaneously by a concerted H migration and the new 3-membered ring formation via TS10 with a barrier of 364 kJ mol^{-1}. C_6H_4CHOH(^{1}A) can be formed also by a step-wise mechanism via $t$$C_6H_5$COH and TS6 at a much higher energy. The intermediate C_6H_4CHOH(^{1}A) lies above C_6H_5CHO by 248 kJ mol^{-1} and can undergo a further dehydration reaction to yield C < C_6H_4 and H_2O. This process has a high energy barrier (270 kJ mol^{-1}) via TS11 with an overall endothermicity computed to be 429 kJ mol^{-1}. The other direct dissociation radical products, C_6H_4CH and OH, of this intermediate occurs without an intrinsic barrier, but with an endothermicity of 362 kJ mol^{-1}. These intermediates play no significant role in the observed fragmentation dynamics, as discussed in Section III-C-2.

Triplet PES: As shown in Figure 9, the triplet state $C_6H_5CHO(^3A")$ is predicted to lie 307 kJ mol^{-1} above singlet $C_6H_5CHO(^1A')$. Five reactions of $C_6H_5CHO(^3A")$ are considered here as Reactions (10–14):

$$C_6H_5CHO(^3A) \rightarrow C_6H_5CO+H \quad (10)$$

$$\rightarrow C_6H_6CO(^3A) \rightarrow C_6H_6(^3B_{1u})+CO \quad (11)$$

$$\rightarrow C_6H_5+HCO \quad (12)$$

$$\rightarrow C_6H_5COH(^3A) \quad (13)$$

$$\rightarrow cC_6H_4CHOH(^3A) \quad (14)$$

Reaction (10) yields C_6H_5CO+H via TS12 with a barrier of 93 kJ mol^{-1} by H elimination from the carbonyl group. Reaction (11) produces $C_6H_6CO(^3A)$ with a barrier of 99 kJ mol^{-1} via TS13, involving the migration of the H atom from the carbonyl group to the phenyl ring; TS13 is only 6 kJ mol^{-1} higher than TS12 in energy. Intermediate $C_6H_6CO(^3A)$, lying 299 kJ mol^{-1} above $C_6H_5CHO(^1A')$, may decompose into CO+$C_6H_6(^3B_{1u})$ via TS14. Both energies of TS14 and CO+$C_6H_6(^3B_{1u})$ are approximately 362 kJ mol^{-1} above that of $C_6H_5CHO(^1A')$. Reaction (12) yields C_6H_5+HCO via TS15 with a barrier of 115 kJ mol^{-1}. As in the singlet PES, C_6H_5CO may decompose further to C_6H_5+CO via TS7 and HCO may decompose to H+CO via TS8. Reaction (13) is an isomerization from $C_6H_5CHO(^3A")$ to $C_6H_5COH(^3A)$ via TS16, with a barrier of 151 kJ mol^{-1}. From $C_6H_5COH(^3A)$, there are five subsequent channels. The lowest barrier channel is the elimination of the hydroxy H atom of $C_6H_5COH(^3A)$ to produce C_6H_5CO via TS21 with energy 427 kJ mol^{-1} relative to $C_6H_5CHO(^1A')$. The formation of the C_6H_4CH+OH products via $t$$C_6H_4$CHOH is unlikely to occur because of the much higher energies of TS19 and TS20. Although the CO+$C_6H_6(^3B_{1u})$ products may also be connected by TS17 from $C_6H_5COH(^3A)$, the contribution of this channel can be ignored because TS17 is higher than TS14 by 234.1 kJ mol^{-1}. The C_6H_5+COH product channel undergoes a direct C–C bond fission of $C_6H_5COH(^3A)$ with TS18, which is only 15.5 kJ mol^{-1} lower than TS17. The final sub-channel is to form C_6H_5C+OH by a loose transition state process. Clearly this channel is uncompetitive with the other channels because of its great dissociation energy. The final channel is an isomerization reaction producing $c$$C_6H_4$CHOH from C_6H_5CHO. Similar to the mechanisms discussed above for the singlet surface, this

channel can take place via the direct 5-centered transition state (via TS22), the barrier energy of which is 103.2 kJ mol^{-1}. After the H migration, *c*C_6H_4CHOH can further undergo a step-wise dehydration reaction and ring formation with the neighboring carbon radical site via transition states TS22 and TS24, respectively, to form H_2O and $C<C_6H_4$ products; these reactions can give rise to the same radical products as those in the singlet state. This product channel cannot compete with other fragmentation channels as aforementioned.

From the above discussion, one can see that all processes on the triplet surface to produce the same products as in the singlet surface need to overcome barriers higher than those on the singlet surface. For example, production of C_6H_5CO+H occurs on the triplet surface via a tighter TS12 at 400 kJ mol^{-1}, whereas the similar dissociation process on the singlet surface occurs by a loose TS with the dissociation energy of 365 kJ mol^{-1}.

II. Calculations of Microcanonical Rate Coefficients

Calculations of microcanonical rate coefficients for both singlet and triplet reaction channels were performed with the VARIFLEX program[64] based on the microcanonical variational transition-state theory and Rice–Ramsperger–Kassel–Marcus (RRKM) theory[65–68] with Eckart tunneling correction. The moments of inertia and vibrational frequencies of the stationary points calculated with B3LYP/6-311+G(3df, 2p) are available in Table S2 in the Supporting Information;[43] they were used to calculate the densities of states. The energy increment was fixed at 10 cm^{-1} in all calculations of sums and densities of states that were performed with the modified Beyer–Swinehart algorithm.[69]

For the decomposition with loose transition states, the potential curve is assumed to be represented with three parts as described by Miller and Klippenstein.[70] The first part is represented with a Morse function. For the process $C_6H_5CHO(^1A')\rightarrow C_6H_5CO$+H, the Morse function is fitted with the expression $V_1(R)=397.9\{1-\exp[-2.173(R-1.200)]\}^2$ kJ mol^{-1}, in which the C–H distance R is in Å. For the process $C_6H_5CHO(^1A')\rightarrow C_6H_5$+HCO the Morse function is presented with the expression $V_2(R)=437.6\{1-\exp[-2.459(R-1.635)]\}^2$ kJ mol^{-1}. The second part corresponds to the degrees of freedom that are identified as normal-mode vibrations in the separate fragments and is assumed to be the same as for the fragments. The third part is the potential energy for the transitional modes, which is described in terms of a set of internal angles with a sum of products of sinusoidal functions.[70] The coefficients in the expression for the transitional potential as functions of bond distance R are estimated on calculating the appropriate force-constant matrix related to the internal angles at C_6H_5CHO. These matrix elements (F_{ij}) are assumed to decay exponentially as bond distance R increases: $F_{ij}(R)=F_{ij}(R_0)\exp[-\eta(R-R_0)]$, in which η is a decay parameter that is obtained from the force-constant matrix of the internal angles at R_0 and R. Figure S6 in the Supporting Information[43] shows the numbering of atoms to determine the internal angles to define the transitional potentials in the dissociation from the loose transition state. For $C_6H_5CHO(^1A')\rightarrow C_6H_5CO$+H, the internal angles are $\theta_1(\measuredangle H_aC_1C_2)$ and $\theta_2(\measuredangle H_aC_1C_2C_3)$ and corresponding η_1 and η_2 are taken to be approximately 0.389 and 0.227 Å^{-1}, respectively, at R(C–H) = 2.6 Å. For $C_6H_5CHO(^1A')\rightarrow C_6H_5$+HCO, there are five internal angles referred to its transitional potential, which include $\theta_1(\measuredangle C_aC_1C_2)$, $\theta_2(\measuredangle C_aC_1C_2C_3)$, $\theta_3(\measuredangle C_1C_aH_b)$, $\theta_4(\measuredangle H_bC_aC_1C_2)$, and $\theta_5(\measuredangle O_cC_aH_bC_1)$ because fragments C_6H_5 and HCO are all nonlinear structures. Decay parameters η_1, η_2, η_3, η_4, and η_5 of the force-constant matrix related to these angles are approximately 1.677, 1.277, 1.566, 1.720, and 1.417 Å^{-1}, respectively, at R(C–C) = 3.0 Å.

Figure 10 shows the calculated microcanonical rate coefficients of both singlet and triplet reaction channels in the energy range of 350–680 kJ mol^{-1}. In Figure 10a, k_1, k_2, and k_9 for generation of C_6H_6+CO, $C_6H_4CO+H_2$, and C_6H_4CHOH are much smaller than k_3 and k_4 for

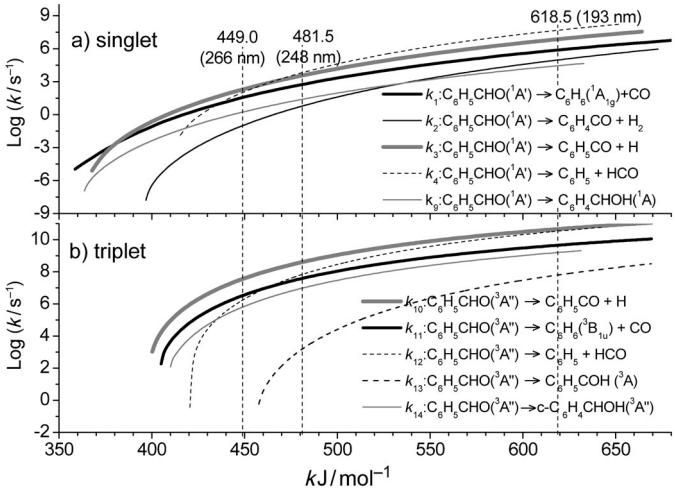

Figure 10. a) Rate coefficients as a function of energy for the singlet decomposition channels of $C_6H_5CHO(^1A')$. b) Rate coefficients as a function of energy for the triplet decomposition channels of $C_6H_5CHO(^3A'')$.

C_6H_5CO+H and C_6H_5+HCO formation, respectively, at $E\geq$ 449 kJ mol^{-1} because Reactions (1) and (2) have tight transition states. Reaction (2) has the smallest rate coefficient among the five channels throughout the energy range investigated. With an energy greater than 460 kJ mol^{-1}, k_4 becomes the largest although Reaction (4) has the largest dissociation energy. At the laser energy of 481.5 kJ mol^{-1} (248 nm), the branching ratios are predicted to be 0.0502, 0.0005, 0.3355, 0.6116, and 0.0022 for Reactions (1)–(4) and (9), respectively. At the laser energy of 618.5 kJ mol^{-1} (193 nm), the branching ratios of Reactions (1)–(4) and (9) become 0.0135, 0.0016, 0.1298, 0.8546, and 0.0005, respectively. Furthermore, because HCO is predicted to eliminate its hydrogen atom to form CO through a barrier of 66.9 kJ mol^{-1}, internally excited HCO radical may further decompose to CO+H. Similarly, C_6H_5CO should also fragment completely into C_6H_5+CO at 193 nm, consistent with

the low C_6H_5CO+H product yield measured experimentally, thus giving mainly C_6H_5+CO+H.

The rate coefficients for the triplet state reactions, k_{10} for C_6H_5CO+H shown in Figure 10b, is predicted to be the largest over the entire energy range, because of its lowest barrier among Reactions (10)–(14). The curve of k_{12} (for C_6H_5+HCO) crosses that of k_{11} (for $C_6H_6(^3B_{1u})$+CO) at about 460 kJ mol^{-1} and k_{12} approaches k_{10} at larger energies. k_{13} (for C_6H_5COH) is the smallest rate coefficient because of the apparently higher barrier of Reaction (13); it is predicted to be zero at the energy 449 kJ mol^{-1} (corresponding to excitation at 266 nm), which is smaller than the threshold energy of TS16. The ratio $k_{10}/k_{11}/k_{12}/k_{14}$ is predicted to be 0.86:0.08:0.05:0.02 at 266 nm. The corresponding ratio at 248 nm is estimated to be 0.82:0.08:0.08:0.02, with that of k_{13} being as low as 3.4×10^{-6}. At 193 nm, the branching ratios of k_{12}, k_{13}, and k_{14} increase to 0.39, 7.3×10^{-4}, and 0.02 whereas those of k_{10} and k_{11} decrease to 0.53 and 0.05. Reactions (10) and (12) are dominant at 193 nm, whereas Reaction (10) dominates at 266 and 248 nm. Rate coefficients (in s^{-1}) of various channels for dissociation of C_6H_5CHO on singlet and triplet surfaces at the experimental excitation energy are listed in Table 1.

Table 1. Rate coefficients (in s^{-1}) of various channels for dissociation of C_6H_5CHO on singlet and triplet surfaces at excitation energy E.

Product channel	450 kJ mol^{-1} (266 nm)	482 kJ mol^{-1} (248 nm)	619 kJ mol^{-1} (193 nm)
Singlet surface			
k_1: C_6H_6+CO	39.4	616	8.2×10^5
k_2: $C_6H_4CO+H_2$	0.1	6.4	9.6×10^4
k_3: C_6H_5CO+H	197	4120	7.9×10^6
k_4: C_6H_5+HCO	103	7510	5.2×10^7
k_9: C_6H_4CHOH	1.9	26.8	2.9×10^4
Triplet surface			
k_{10}: C_6H_5CO+H	3.3×10^7	4.1×10^8	4.6×10^{10}
k_{11}: $C_6H_6(^3B_{1u})$+CO	3.0×10^6	4.1×10^7	4.6×10^9
k_{12}: C_6H_5+HCO	1.8×10^6	4.2×10^7	3.4×10^{10}
k_{13}: $C_6H_5COH\rightarrow C_6H_5COH$	0	1.7×10^3	6.3×10^7
k_{14}: $C_6H_5COH\rightarrow cH_4CHOH$	6.8×10^5	1.0×10^7	1.6×10^9

To depict the evolution of the species in the C_6H_5CHO decomposition, we performed kinetic modeling at 266 nm and 193 nm; the results are shown in Figure 11a and b, respectively, based on the major reaction channels shown in Figures 8 and 9. The rate coefficients of both $C_6H_5CHO(S_1)\rightarrow C_6H_5CHO(^3A'')$ and $C_6H_5COH(^1A')\rightarrow C_6H_5COH(^3A)$ are taken to be the experimental value of 2.4×10^{10} s^{-1} from the literature.[41] In the simulation, the rate of internal conversion has been convoluted to give a 15 ns decay time (HWFM) for PhCHO.

In Figure 11a, for photolysis at 266 nm, the branching ratio of C_6H_5CHO decreases by fragmentation whereas that of H+C_6H_5CO increases gradually with time and reaches a plateau at 300 ns. That of $C_6H_5CHO(^3A'')$ grows rapidly at the beginning of the reaction and reaches a maximum at approximately 30 ns before decaying gradually to zero in

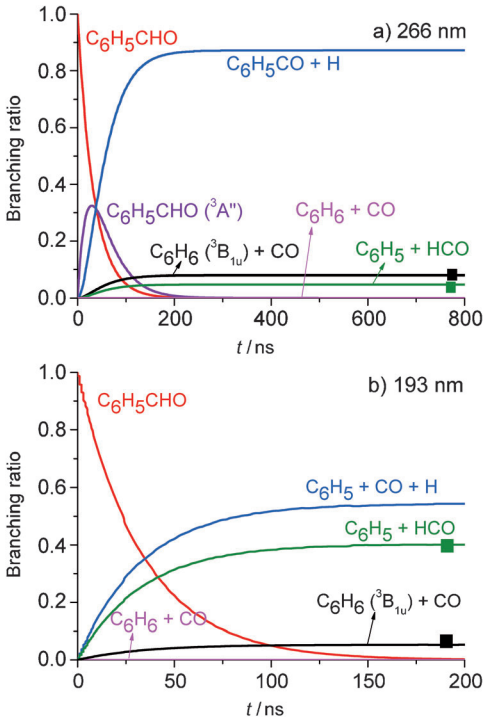

Figure 11. a) Branching ratios of species, red: C_6H_5CHO, purple: $C_6H_5CHO(^3A'')$, blue: C_6H_5CO+H, black: $C_6H_6(^3B_{1u})$+CO, green: C_6H_5+HCO, magenta: C_6H_6+CO in the kinetic modeling of C_6H_5CHO decomposition at 266 nm and b) branching ratio of species, red: C_6H_5CHO, blue: C_6H_5+CO+H, green: C_6H_5+HCO, black: $C_6H_6(^3B_{1u})$+CO, and magenta: C_6H_6+CO in the kinetic modeling of C_6H_5CHO decomposition at 193 nm. The squares represent the relative branching ratios for HCO (black) and CO (olive) elimination channels from experimental measurement; H atom elimination channel is not included owing to the large uncertainly.

about 300 ns through isomerization and decomposition. The branching ratios of C_6H_5CO+H, $C_6H_6(^3B_{1g})$+CO, C_6H_5+HCO, and C_6H_6+CO are 0.87, 0.08, 0.05, 0.00, respectively. The branching ratios of species upon photolysis at 193 nm, shown in Figure 11b, differ greatly from those at 266 nm. The relative concentration of C_6H_5CHO decays and approaches zero more rapidly than that at 266 nm as expected. The branching ratios of the three product species increase rapidly in less than 100 ns; their values reach a plateau at $t>200$ ns. The main products at 193 nm are therefore predicted to be C_6H_5+CO+H (via C_6H_5CO), C_6H_5+HCO, and CO with a small proportion of C_6H_6; the calculated branching ratios for Reactions (1), (3), and (4) are 0.05, 0.54, and 0.40. The major channel at 266 nm is predicted to be Reaction (3), whose branching ratio cannot be determined experimentally. However, the prediction that the product channel C_6H_6+CO is more important than the C_6H_5+HCO channel is consistent with the experimental observation of the ratio 4.1 ± 0.3 to 1.0 ± 0.1.

We also predicted the transient intermediate species of the C_6H_5CHO reaction system; the most significant intermediate is $cC_6H_4CHOH(^3A'')$. However, the branching ratios of C_6H_4CHOH following excitation at 266 nm or

193 nm are less than 5.7×10^{-3} and 8.5×10^{-5}, respectively, so that their contributions to the detected photofragmentation products are negligible. We have also modeled the product yields following ps- or fs-laser excitation at 266 nm using the intersystem crossing rate of $2.4\times10^{10}\,s^{-1}$ reported by Park and co-workers,[41] who detected a triplet-state "quinoid-like" intermediate in their ultrafast electron-diffraction experiment on benzaldehyde. Although the time evolution of the triplet benzaldehyde (which is controlled solely by the intersystem crossing dynamics) could be quantitatively modeled, the CO+C_6H_6 product evolution reported by these authors could not be accounted for by our detailed mechanisms depicted in Figures 8 and 9. We found that the product distribution following the 15 ns laser photolysis at 266 nm is contributed primarily from H+C_6H_5CO and $C_6H_5CHO(^3A'')$ formation.

Discussion

According to theoretical calculations and our experimental results, Reaction (2) for elimination of H_2 is unimportant. The results of the experiments are thus summarized according to the following Reactions 15–23:

$$C_6H_5CHO+h\nu \rightarrow C_6H_5CHO^{**} \quad (15)$$

$$C_6H_5CHO^{**} \rightarrow C_6H_5CHO(^3A) \quad (16)$$

$$C_6H_5CHO^{**} \rightarrow C_6H_5CHO(^1A') \quad (17)$$

$$C_6H_5CHO(^3A) \rightarrow C_6H_5CO+H \quad (18)$$

$$C_6H_5CO \rightarrow C_6H_5+CO \text{ (for 193 nm)} \quad (19)$$

$$C_6H_5CHO(^3A) \rightarrow C_6H_5+HCO \quad (20)$$

$$C_6H_5CHO(^3A) \rightarrow C_6H_6(^3B_{1u})+CO \quad (21)$$

$$C_6H_5CHO(^1A') \rightarrow C_6H_5+HCO \quad (22)$$

$$C_6H_5CHO(^1A') \rightarrow C_6H_5CO+H \quad (23)$$

in which $C_6H_5CHO^{**}$ represents the initially excited state; irradiation at 266, 248, and 193 nm is expected to excite C_6H_5CHO to its S_2, S_2, and S_7 states, respectively. The populations in the initially excited states are mainly transferred to the ground electronic state and the triplet state through internal conversion and intersystem crossing, respectively. Reactions (18), (20), and (21) represent the channels with H, HCO, and CO elimination from the triplet state. Reactions (22) and (23) represent the HCO and H elimination from the ground state, respectively. The dissociation rate of Reactions (22) and (23) are only large enough at 193 nm such that the elimination occurs in our observation time window.

The disk-like image observed at 248 nm and 266 nm indicates that benzaldehyde dissociates into fragments incompletely even after 100 μs. The very slow dissociation rates at 248 and 266 nm in the ground state predicted by calculations suggest the disk-like images result from the dissociative ionization of the undissociated internally excited C_6H_5CHO in its ground electronic state. The incomplete dissociation is also consistent with observation of IR emission near 2730, 2810, and 3070 cm^{-1} assigned to emission from internally excited C_6H_5CHO in the period 50–75 μs upon photolysis at 193 nm with added Ar quencher. In principle, the internally excited C_6H_5CHO in its ground electronic state can derive its population from intersystem crossing via the T_1 state or internal conversion from the initial excited singlet states.

We discuss the major channels, Reactions (18)–(23), as follows.

The C_6H_5+HCO Channel: The multi-mass ion imaging experiments indicate that this channel is the major channel for photolysis at 193 nm and at least two dissociation channels are involved because a minor slow component and a major rapid component in translational energy distribution were observed. According to the theoretical predictions on branching ratios, these two channels might correspond to dissociation on the singlet and triplet surfaces, with the latter as the major channel. Dissociation on the singlet surface is direct, whereas dissociation on the triplet surface involves a small exit barrier; observation of the major rapid component is consistent with dissociation on the triplet surface.

Emission of HCO from levels $v=1$ and 2 of ν_3 (C–O stretching) and $v=1$ of ν_1 (C–H stretching) modes was observed upon photolysis of C_6H_5CHO at 193 nm. Because the Einstein coefficients for vibronic levels of HCO are lacking, we can only provide an estimated upper limit of 20 kJ mol^{-1} for the internal energy of HCO. Combining the observed average translational energy of approximately 30 kJ mol^{-1} and this upper limit for internal energy of HCO, most available energy (199 kJ mol^{-1}) upon photolysis at 193 nm is clearly distributed to the internal energy of C_6H_5.

As the excitation wavelength is increased to 248 and 266 nm, the decomposition rate coefficient of this channel decreased much more rapidly than other channels, as shown in Figure 10; the branching of this channel is hence decreased, consistent with our experimental observation. Upon photolysis at 248 nm, the available energy is approximately 68 kJ mol^{-1}. With the observed average translational energy of 25 kJ mol^{-1}, only 43 kJ mol^{-1} remains for distribution among the internal energies of HCO and C_6H_5. Observation of weak emission mainly from the $v=1$ level (ca. 22 kJ mol^{-1}) of the C=O stretching mode is consistent with these considerations.

The C_6H_6+CO Channel: Quantum-chemical computations predict that the channel C_6H_6+CO comes mainly from the triplet state and C_6H_6 is generated in the triplet state $^3B_{1u}$. The small translational energy of CO observed at all excitation wavelengths indicates that formation of CO is mainly from the triplet surface, because TS1 on the singlet surface has a very large reverse barrier.

Emission of CO from $v \leq 2$, $J \leq 43$, and ions of $m/z = 78$ were observed, with similar internal energy distributions observed at 248 nm and 193 nm. Combining the observed average translational energy of approximately 38 kJ mol^{-1} and the average internal energy of approximately 19 kJ mol^{-1} for internal energy of CO upon photolysis of C_6H_5CHO at 193 nm, 201 kJ mol^{-1} remains to be distributed to the internal energy of C_6H_6 if triplet C_6H_6 is produced. For photolysis of C_6H_5CHO at 248 nm, the observed average translational energy is approximately 27 kJ mol^{-1} and the average internal energy of CO is approximately 21 kJ mol^{-1}. If triplet C_6H_6 were produced, its internal energy would be 72 kJ mol^{-1}.

The dissociation lifetime of benzene with internal energy 618.6 kJ mol^{-1} (193 nm) is 10 μs, and becomes greater than 300 μs with internal energy 480 kJ mol^{-1} (248 nm).[71] If highly internally excited benzene in the ground state is produced, it easily fragments into ions with $m/z = 77$, 52, 50, and 39 upon ionization. As we only observed a very small signal at $m/z = 52$, 50, and 39, a large fraction of benzene is likely produced in the triplet state. This is consistent with the quantum-chemical computations.

The production of triplet C_6H_6 is consistent with previous reports by Silva and Reilly who observed C_6H_6 ions with a probe laser at 157 nm that has energy sufficient to ionize triplet C_6H_6 but not C_6H_6 in its ground state.[39] Park and coworkers indicated also that, upon irradiation at 266.7 nm, C_6H_5CHO was excited to the S_2 state, followed by relaxation to the S_1 state that subsequently underwent bifurcation, and some reactions proceeded via the triplet surface to produce triplet C_6H_6+CO.[41] They also observed some formation of C_6H_6+CO through the singlet channel; even though previous literature indicated that intersystem crossing $S_1 \rightarrow T_1$ has an efficiency near unity.[23–24]

The C_6H_5CO+H Channel: Quantum-chemical computations predict that channel C_6H_5CO+H has similar branching ratio to that of C_6H_5+HCO at 193 nm. It is more enhanced at 248 and 266 nm. This channel comes mainly from the triplet state, and the product C_6H_5CO is predicted to further decompose into C_6H_5+CO at 193 nm. However, the multimass ion imaging experiments indicate that this channel is minor, with a branching ratio estimated to be 0.05 upon excitation at 193 nm, and the branching ratios at 248 and 266 nm cannot be determined. The difference between our experimental results and theoretical calculations at 193 nm can be attributed to two possible factors. First, as we did not observe C_6H_5CO radicals, it indicates all C_6H_5CO decomposes into C_6H_5+CO. Only the extra component of C_6H_5 in the momentum match between C_6H_5 and HCO is attributed to the C_6H_5 from the secondary decomposition $C_6H_5CO \rightarrow C_6H_5$+CO. If some of the C_6H_5 from the secondary decomposition is buried in the C_6H_5 generated from the primary channel $C_6H_5CHO \rightarrow C_6H_5$+HCO, then the branching ratio of the H-atom elimination channel is underestimated. Second, the intersystem crossing rate we used in the calculation was obtained at 266 nm in a previous study.[41] However, this value maybe very different at 193 nm. If intersystem crossing rate at 193 nm decreases, then the branching ratio of H-atom elimination channel decreases and the HCO elimination increases.

The experimental measurement and theoretical calculations show the same trend in the changes of branching ratios with photon energy. However, the predictions of branching ratios are not very accurate. Nowadays, potential-energy surfaces can be calculated with reasonable accuracy even for the electronic excited states. Statistical calculations with RRKM theory can predict branching ratios of dissociation channels on a single potential-energy surface quite well if the total energy in the molecule is not much larger than the dissociation thresholds. However, the branching ratio calculations are not that accurate if the total energy in the molecule is much larger than the dissociation thresholds (like 193 nm photon energy in this work) owing to the vibrational anharmonicity. The calculations of the densities of states and total number of states at the transition state based on harmonic oscillators produce significant errors in RRKM calculations for molecules with large energy. An additional calculation inaccuracy may come from the coupling between different potential-energy surfaces. The calculation of coupling is not that straightforward and it makes the predictions of branching ratios between different surfaces difficult. In this work, we did not calculate the coupling between singlet and triplet potential-energy surfaces. We simply use the intersystem crossing rate at 266 nm from a previous experimental measurement. This could make the prediction of branching ratios at 193 nm more different from experimental results.

Conclusions

The dissociation of C_6H_5CHO upon UV excitation involves several channels. Some C_6H_5CHO does not dissociate within 100 μs at 248 or 266 nm; and IR emission of C_6H_5CHO from internally excited states were observed. The C_6H_5+HCO channel has two components, each with large and small photofragment recoil velocities, respectively, although the rapid component dominates. According to theoretical computations, the major channel involves dissociation on the triplet surface, whereas the minor channel on the singlet surface. Emission of HCO was observed; upon photolysis of C_6H_5CHO at 193 nm, HCO has more internal excitation than at 248 nm.

According to calculations, the C_6H_6+CO channel proceeds mainly on the triplet surface so a majority of C_6H_6 is in its triplet state, consistent with experimental observation. At 248 or 266 nm, the C_6H_6+CO channel is more important than the C_6H_5+HCO channel, whereas the C_6H_5+HCO channel becomes the major channel at 193 nm. The C_6H_5+HCO channel has an average translational energy of 30, 25, and 20 kJ mol^{-1} and the C_6H_6+CO channel has an average translational energy of 38, 27, and 22 kJ mol^{-1} upon irradiation of C_6H_5CHO at 193, 248, and 266 nm, respectively. Emission of CO ($v \leq 2$, $J \leq 43$) with similar internal distri-

butions was observed at both 248 and 193 nm, with average rotational energy of approximately 13 kJ mol^{-1} and vibrational energy approximately 6 kJ mol^{-1}. The C_6H_5CO+H channel is the least important of these three dissociation channels.

Experimental Section

Multimass Ion Imaging

As the experimental techniques have been described in detail previously,[71–73] only a brief description is given here. C_6H_5CHO vapor was prepared by flowing ultra pure Ne at a pressure of 250 Torr through a reservoir containing liquid C_6H_5CHO at 323 K. The C_6H_5CHO/Ne mixture was then expanded through a pulsed nozzle (diameter 500 μm) to form a molecular beam. Molecules in that beam were photodissociated with light from a pulsed UV laser. The resulting photofragments were ionized with a pulsed VUV laser beam at 118 nm. Photofragment masses were identified along with their translational energy distributions using multimass ion imaging techniques.

Time-resolved Fourier-transform Spectra

The apparatus employed to obtain step-scan time-resolved Fourier-transform spectra (TR-FTS) has been described previously.[74–76] The sizes of the photolysis beams at the detection center were approximately 7.5 × 6.5 mm^2 with a fluence of around 22 mJ cm^{-2} from an ArF laser at 193 nm (Gam laser, EX100H/60) and approximately 9 × 10 mm^2 with a fluence around 89 mJ cm^{-2} from a KrF laser at 248 nm (Lambda Physik, LPX200). The transient signal detected with an InSb detector (rise time 0.22 μs) was preamplified, followed by further amplification by a factor of 100 (bandwidth 1 MHz) before being digitized with an external data-acquisition board (12-bit ADC) with a resolution of 50 ns. A filter (OCLI, W05200-6X) passing 1670–2330 cm^{-1} was used for undersampling. Data were typically averaged over 60 laser pulses at each scan step; 4239 scan steps were performed to yield an interferogram resulting in a spectrum with a resolution of 0.4 cm^{-1} in the spectral region of 1850–2330 cm^{-1}. To improve the signal to noise (S/N) ratio of the spectrum, 20 consecutive time-resolved spectra were summed to yield spectra representing emission at intervals of 1.0 μs.

Benzaldehyde was injected into the vacuum chamber as a diffusive beam through a slit-shaped inlet. The sample was heated to about 325 K at which temperature its vapor pressure is approximately 5.6 Torr.[77] The partial pressure of C_6H_5CHO in the chamber was maintained under 31 mTorr for experiments at 193 nm and 37 mTorr for 248 nm.

He (Scott Specialty Gases, 99.999%) in a minimal amount (ca. 24 mTorr for experiments at 193 nm and ca. 75 mTorr for 248 nm) was added near the entrance of the photolysis port to suppress the formation of a solid deposit on the quartz window. C_6H_5CHO (Aldrich, ≧99%) was used without purification except for degassing; no impurity was detected in its IR spectrum.

Acknowledgements

National Science Council of Taiwan (NSC Grant No. NSC99-2745M009-001-ASP and NSC 97-2628M-001-MY3) and the Ministry of Education, Taiwan ("Achieving Top Universities Program" of National Chiao Tung University) supported this work. M.C.L. acknowledges the support by NSC as well as TSMC (Taiwan Semiconductor Manufacturing Co.) for distinguished professorship at NCTU and Z.F.X. thanks NSC for the support as a visiting scientist at NCTU.

[1] C. L. Wilson, J. M. Solar, A. El Ghaouth, D. R. Fravel, *Hortscience* **1999**, *34*, 681–685.
[2] R. Atkinson, S. M. Aschmann, J. Arey, *Int. J. Chem. Kinet.* **1991**, *23*, 77–97.
[3] R. Atkinson, *J. Phys. Chem. Ref. Data Monograph* **1994**, No. 2.
[4] B. Klotz, S. Sorensen, I. Barnes, K. H. Becker, T. Etzkorn, R. Volkamer, U. Platt, K. Wirtz, M. Martin-Reviejo, *J. Phys. Chem. A* **1998**, *102*, 10289–10299.
[5] D. F. Smith, T. E. Kleindienst, C. D. McIver, *J. Atmos. Chem.* **1999**, *34*, 339–364.
[6] J. G. Calvert, R. Atkinson, K. H. Becker, R. M. Kamens, J. H. Seinfeld, T. J. Wallington, G. Yarwood in *The Mechanisms of Atmospheric Oxidation of Aromatic Hydrocarbons*, Oxford University Press, London, UK, **2002**.
[7] E. Christophy, K. Myli, T. R. Viegut, J. A. Rzepiela, J. M. Hossenlopp, *J. Photochem. Photobiol. A* **1997**, *110*, 229–234.
[8] S. N. Dubtsov, G. G. Dultseva, E. N. Dultsev, G. I. Skubnevskaya, *J. Phys. Chem. B* **2006**, *110*, 645–649.
[9] F. Caralp, V. Foucher, R. Lesclaux, T. J. Wallington, M. D. Hurley, *Phys. Chem. Chem. Phys.* **1999**, *1*, 3509–3517.
[10] H. Abe, S. Kamei, N. Mikami, M. Ito, *Chem. Phys. Lett.* **1984**, *109*, 217–220.
[11] J. Smolarek, R. Zwarich, L. Goodman, *J. Mol. Spectrosc.* **1972**, *43*, 416–428.
[12] D. G. Leopold, R. J. Hemley, V. Vaida, J. L. Roebber, *J. Chem. Phys.* **1981**, *75*, 4758–4769.
[13] K. Kimura and S. Agakura, *Theor. Chim. Acta* **1965**, *3*, 164–173.
[14] C. R. Silva, J. P. Reilly, *J. Phys. Chem.* **1996**, *100*, 17111–17123.
[15] V. Molina, M. Merchan, *J. Phys. Chem. A* **2001**, *105*, 3745–3751.
[16] M. Berger, I. L. Goldblatt, C. Steel, *J. Am. Chem. Soc.* **1973**, *95*, 1717–1725.
[17] N. Ohmori, T. Suzuki, M. Ito, *J. Phys. Chem.* **1988**, *92*, 1086–1093.
[18] E. Villa, A. Amirav, W. Chen, E. C. Lim, *Chem. Phys. Lett.* **1988**, *147*, 43–48.
[19] O. Sneh, O. Cheshnovsky, *J. Phys. Chem.* **1991**, *95*, 7154–7164.
[20] M. Koyanagi, L. Goodman, *Chem. Phys.* **1979**, *39*, 237–250.
[21] J. M. Hollas. S. N. Thakur, *Chem. Phys.* **1973**, *1*, 385–391.
[22] L. Goodman, M. Koyanagi, *Mol. Photochem.* **1972**, *4*, 369–415.
[23] U. Brühlmann, J. R. Huber, *Chem. Phys. Lett.* **1979**, *66*, 353–357.
[24] T. Itoh, *Chem. Phys. Lett.* **1988**, *151*, 166–168.
[25] M. Biron, P. Longin, *Chem. Phys. Lett.* **1985**, *116*, 250–253.
[26] T. Itoh, T. Takemura, H. Baba, *Chem. Phys. Lett.* **1976**, *40*, 481–483.
[27] T. Itoh, *Chem. Phys. Lett.* **1987**, *133*, 254–258.
[28] Y. Hirata, E. C. Lim, *J. Chem. Phys.* **1980**, *72*, 5505–5510.
[29] *Handbook of Chemistry and Physics*, CRC Press, Boca Raton, FL, USA, **1997**.
[30] W. D. Good, N. K. Smith, *J. Chem. Eng. Data* **1969**, *14*, 102–106.
[31] S. G. Lias, J. E. Bartmess, J. F. Liebman, J. L. Holmes, R. D. Levin, W. G. Mallard, *J. Phys. Chem. Ref. Data* **1988**, *17*, S1.
[32] R. K. Solly, S. W. Benson, *J. Am. Chem. Soc.* **1971**, *93*, 1592–1595.
[33] M. W. Chase, Jr., *J. Phys. Chem. Ref. Data Monograph* **1998**, *9*, 1–1951.
[34] U. Brühlmann, M. Monella, P. Russegger, J. R. Huber, *Chem. Phys.* **1983**, *81*, 439–447.
[35] M. B. Robin, N. A. Kuebler, *J. Am. Chem. Soc.* **1975**, *97*, 4822–4825.
[36] J. J. Yang, D. A. Gobeli, M. A. El-Sayed, *J. Phys. Chem.* **1985**, *89*, 3426–3429.
[37] J. J. Yang, D. A. Gobeli, R. S. Pandolfi, M. A. El-Sayed, *J. Phys. Chem.* **1983**, *87*, 2255–2260.
[38] S. R. Long, J. T. Meek, P. J. Harrington, J. P. Reilly, *J. Chem. Phys.* **1983**, *78*, 3341–3343.
[39] C. R. Silva, J. P. Reilly, *J. Phys. Chem. A* **1997**, *101*, 7934–7942.
[40] L. Zhu, T. J. Cronin, *Chem. Phys. Lett.* **2000**, *317*, 227–231.
[41] S. T. Park, J. S. Feenstra, A. H. Zewail, *J. Chem. Phys.* **2006**, *124*, 174707-1–174707-23.
[42] S. K. Shin, H. L. Kim, C. R. Park, *Bull. Korean Chem. Soc.* **2002**, *23*, 286–290.
[43] See the Supporting Information for ion images from photolysis of C_6H_5CHO at 193, 248, and 266 nm, IR emission spectra of CO at resolution of 0.4 cm^{-1}, structures of reactant, products, and transi-

tion states, and numbering of atoms to define transitional potentials in dissociation processes.
[44] G. El Dib, A. Chakir, E. Roth, J. Brion, D. Daumont, *J. Phys. Chem. A* **2006**, *110*, 7848–7857.
[45] J. F. Ogilvie, S.-L. Cheah, Y.-P. Lee, S. P. A. Sauer, *Theor. Chem. Acc.* **2002**, *108*, 85–97.
[46] J. F. Ogilvie in *The Vibrational and Rotational Spectrometry of Diatomic Molecules*, Academic Press, London, UK, **1998**.
[47] J. M. Brown, J. Buttenshaw, A. Carrington, K. Dumper, C. R. Parent, *J. Mol. Spectrosc.* **1980**, *79*, 47–61.
[48] C. B. Dane, D. R. Lander, R. F. Curl, F. K. Tittel, Y. Guo, M. I. F. Ochsner, C. B. Moore, *J. Chem. Phys.* **1988**, *88*, 2121–2128.
[49] A. R. W. McKellar, J. B. Burkholder, J. J. Orlando, C. J. Howard, *J. Mol. Spectrosc.* **1988**, *130*, 445–453.
[50] C. M. Western, *PGOPHER*, a program for simulating for rotational structure; http://pgopher.chm.bris.ac.uk.
[51] J. D. Tobiason, J. R. Dunlop, E. A. Rohlfing, *J. Chem. Phys.* **1995**, *103*, 1448–1469.
[52] http://webbook.nist.gov/cgi/cbook.cgi?ID=C71432&Units=SI.
[53] E. N. Sharp, M. A. Roberts, D. J. Nesbitt, *Phys. Chem. Chem. Phys.* **2008**, *10*, 6592–6596.
[54] R. J. McMahon, M. C. McCarthy, C. A. Gottlieb, J. B. Dudek, J. F. Stanton, P. Thaddeus, *Astrophys. J.* **2003**, *590*, L61–L64.
[55] A. V. Friderichsen, J. G. Radziszewski, M. R. Nimlos, P. R. Winter, D. C. Dayton, D. E. David, G. B. Ellison, *J. Am. Chem. Soc.* **2001**, *123*, 1977–1988.
[56] A. D. Becke, *J. Chem. Phys.* **1993**, *98*, 5648–5652.
[57] A. D. Becke, *J. Chem. Phys.* **1992**, *96*, 2155–2160.
[58] A. D. Becke, *J. Chem. Phys.* **1992**, *97*, 9173–9177.
[59] C. Lee, W. Yang, R. G. Parr, *Phys. Rev.* **1988**, *37B*, 785–794.
[60] R. E. Stratmann, G. E. Scuseria, M. J. Frisch, *J. Chem. Phys.* **1998**, *109*, 8218–8224.
[61] J. A. Pople, M. Head-Gordon, K. Raghavachari, *J. Chem. Phys.* **1987**, *87*, 5968–5975.
[62] G. E. Scuseria, H. F. Schaefer, III, *J. Chem. Phys.* **1989**, *90*, 3700–3703.
[63] Gaussian 03, Revision C.01, M. J Frisch et al., Gaussian, Inc., Wallingford, CT, USA, **2004**.
[64] S. J. Klippenstein, A. F. Wagner, R. C. Dunbar, D. M.Wardlaw, S. H. Robertson, *VARIFLEX Version 1.00*, **1999**.
[65] D. M. Wardlaw, R. A. Marcus, *Chem. Phys. Lett.* **1984**, *110*, 230–234.
[66] D. M. Wardlaw, R. A. Marcus, *J. Chem. Phys.* **1985**, *83*, 3462–3480.
[67] S. J. Klippenstein, *J. Chem. Phys.* **1992**, *96*, 367–371.
[68] S. J. Klippenstein, R. A. Marcus, *J. Chem. Phys.* **1987**, *87*, 3410–3417.
[69] D. C. Astholz, J. Troe, W. Wieters, *J. Chem. Phys.* **1979**, *70*, 5107–5116.
[70] J. A. Miller, S. J. Klippenstein, *J. Phys. Chem. A* **2000**, *104*, 2061–2069.
[71] S.-T. Tsai, C. K. Lin, Y. T. Lee, C. K. Ni, *J. Chem. Phys.* **2000**, *113*, 67–70.
[72] S.-T. Tsai, C. K. Lin, Y. T. Lee, C.-K. Ni, *Rev. Sci. Instrum.* **2001**, *72*, 1963–1969.
[73] C. K. Ni, Y. T. Lee, *Int. Rev. Phys. Chem.* **2004**, *23*, 187–218.
[74] P. S. Yeh, G. H. Leu, Y. P. Lee, I-C Chen, *J. Chem. Phys.* **1995**, *103*, 4879–4886.
[75] S. R. Lin, Y. P Lee, *J. Chem. Phys.* **1999**, *111*, 9233–9241.
[76] C. Y. Wu, Y. J. Wu, Y. P Lee, *J. Chem. Phys.* **2004**, *121*, 8792–8799.
[77] D. R. Stull, *Ind. Eng. Chem.* **1947**, *39*, 517–540.

Received: May 25, 2011
Published online: September 23, 2011

